Dual-Active-Bridge Based Self-Balancing DC–DC Converter With Coupled Inductor for Bipolar DC Microgrids

Guangfu Ning, *Member, IEEE*, Ribo Zhang, *Graduate Student Member, IEEE*, Li Jiang, *Member, IEEE*,
Yonglu Liu, *Member, IEEE*, Yao Sun, *Member, IEEE*, and Mei Su, *Member, IEEE*

***Abstract*—Although bipolar dc microgrids exhibit enhanced reliability and transmission efficiency compared to unipolar dc microgrids, they are prone to voltage imbalance issues. This article proposes a dual active bridge (DAB) based bipolar dc–dc converter with coupled inductors to automatically balance bipolar output voltages under any load conditions. The proposed converter can operate with a simple single phase-shift modulation. Moreover, the coupled inductor is the key to realize self-balancing and roles as the power transfer inductor as well. The zero-voltage-switching can also be achieved for all switches under different load conditions. The operation and self-balancing principles are analyzed in detail. The characteristics of the proposed converter are well verified by a 1 kW prototypes under different load conditions.**

***Index Terms*—Bipolar dc microgrid, coupled inductor, dual active bridge (DAB), voltage imbalance, zero-voltage switching (ZVS).**

I. INTRODUCTION

DISTRIBUTED energy sources (DESs) like wind and solar offer clean energy but require solutions for intermittency [1]. DC microgrids address this challenge through direct renewable integration, with bipolar configurations (three-wire) outperforming unipolar configurations (two-wire) by providing dual voltage levels for enhanced efficiency and reliability [2], [3]. A typical bipolar dc microgrid is depicted in Fig. 1. However, the asymmetry between dc poles caused by unbalanced loads or DESs may result in the problem of bipolar voltage imbalance, which will deteriorate power quality and grid safety [4], [5].

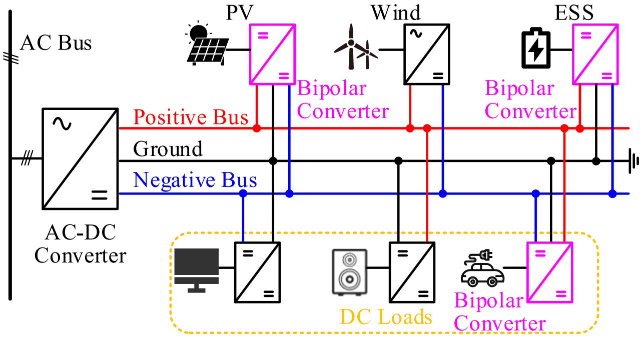

Fig. 1. Block diagram of the bipolar DC microgrid.

Therefore, a series of independent voltage balancers have been proposed to alleviate the bipolar voltage imbalance problem [6], [7], [8]. For example, a simple buck/boost-type voltage balancer was proposed in [6], but its topology is prone to the shoot-through problem. Thus, Zhang and Gong [7] proposed a dual-buck half-bridge voltage balancer, which effectively prevents the shoot-through of the bridge arms in the converter. In addition, a three-level voltage balancer is proposed for high dc voltage application [8]. However, the two-stage structure requires more devices, which reduces its power conversion efficiency and power density. Hence, advanced converters integrate the voltage balancer into the dc/dc converter, which could be roughly divided into non-isolated and isolated solutions.

For nonisolated solutions, Tavakoli et al. [9] proposed a converter that can alleviate voltage balance by feeding power into the bipolar dc bus. A three-level-boost is proposed in [10], which can achieve automatic voltage balancing and high gain, but it suffers from hard switching and high component count. In [11], a hybrid sepic-boost converter is proposed, which can achieve zero-voltage-switching (ZVS). Both papers [10] and [11] have the problem of large number of components. A bipolar converter in [12] uses only a single inductor, but it cannot achieve self-balancing. Therefore, a more complex control strategy is required. In contrast, the topology in [13] has fewer components, and self-balancing and ZVS can be achieved. Without galvanic isolation, common-mode voltages will create low impedance paths between the dc ground, over which large fault currents will flow thus reducing the safety of the equipment [14]. In addition, most nonisolated bipolar converter face the contradiction of high voltage gain and low component count [15], [16].

Compared with nonisolated solutions, the isolated solutions demonstrate enhanced safety and reliability. An interleaved

---

Received 11 April 2025; revised 28 June 2025; accepted 26 July 2025. Date of publication 31 July 2025; date of current version 8 September 2025. This work was supported in part by the National Natural Science Foundation of China under Grant 52477207, Grant 52307231, Grant U23B20129, and Grant 62125308, and in part by the Hunan Provincial Natural Science Foundation of China under Grant 2024JJ1011. Recommended for publication by Associate Editor E. Lee. *(Corresponding author: Li Jiang.)*

The authors are with the School of Automation, Central South University, Changsha 410083, China, and also with the Hunan Provincial Key Laboratory of Power Electronics Equipment and Grid, Changsha 410083, China (e-mail: ningguangfu@csu.edu.cn; 244612234@csu.edu.cn; jianglicsu@csu.edu.cn; liuyonglu@csu.edu.cn; yaosun@csu.edu.cn; sumeicsu@csu.edu.cn).

Color versions of one or more figures in this article are available at https://doi.org/10.1109/TPEL.2025.3594430.

Digital Object Identifier 10.1109/TPEL.2025.3594430

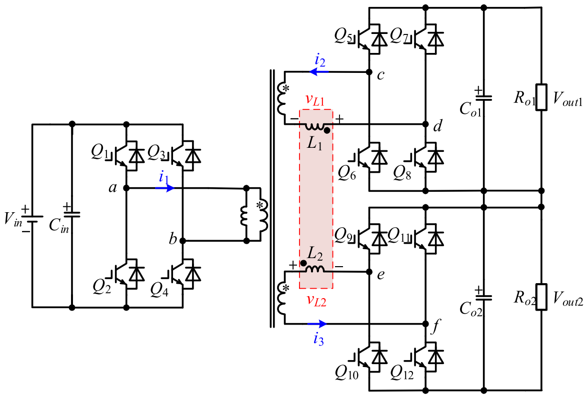

Fig. 2. Bipolar TAB converter based on coupled inductor in [25].

balancing inductor is added to the *CLLC* bidirectional dc/dc converter to achieve voltage balancing in [17]. However, it contains a large number of passive components, resulting in larger size and lower efficiency. A coupled-inductor-based buck-type converter is proposed in [18], which reserves the wide voltage gain range of traditional buck converter, but it suffers from high component count and switching losses. Following that, Lin et al. [19] proposed bipolar current-fed dc–dc converter, which not only have the advantage of low input current ripples, but also achieve full range ZVS. The dual-active-bridge (DAB) converter is a very popular topology for isolated bipolar dc/dc converter due to its ZVS capability and seamless power control capability [20], [21]. Therefore, more and more scholars are focusing on bipolar self-balancing converters based on DAB topology. An isolated four port voltage self-balancing converter based on DAB is proposed by using a high frequency branch [22], which ensures the safety of the system. However, it cannot achieve self-balancing, and thus a more complex control strategy is required. In [23], an automatic voltage-balancing bipolar converter is proposed, which can achieve a wide voltage gain range and ZVS over the full load range. However, two bulky dc inductors will increase the size of the device while reducing the power while reducing the power density. To obtain a smaller device size, magnetic integration technology is widely used. In [24], a voltage balancing for triple-active-bridge (TAB) converter using integrated transformer is proposed. Moreover, Naseem and Cha [25] proposed bipolar TAB converter with automatic voltage balancing by using coupled inductor, as shown in Fig. 2. Compared with paper [23], it requires only two magnetic components, thus offering smaller device size. However, it has four more switches than the traditional DAB converter, which will increase greater switching losses.

Based on paper [25], this article proposes a self-balancing DAB converter with coupled inductor to eliminate the aforementioned drawbacks, as shown in Fig. 3. The proposed converter has the following advantages:

1) It can balance the output voltages regardless of load conditions.
2) Compared with the conventional DAB, the coupled inductor provides the required inductance for power transfer, and the ZVS can be achieved for all switches under different load conditions.
3) The number of semiconductor devices is reduced by four compared to the converter in [25]; hence, switching losses can be significantly reduced.
4) A simple single phase-shift modulation can be used to operate the proposed converter.

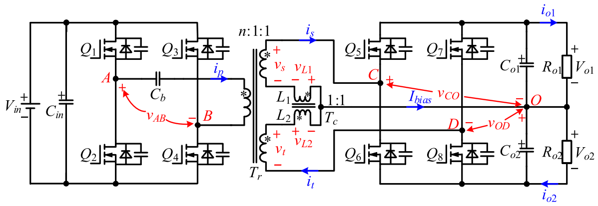

Fig. 3. Proposed converter.

II. PROPOSED TOPOLOGY AND OPERATION PRINCIPLES

The proposed DAB based bipolar converter is shown in Fig. 3, which can be implemented by adopting three-winding high-frequency transformer (T_r) and split output filter capacitors (C_{o1} and C_{o2}), and adding one coupled inductor to the traditional DAB converter (four primary switches Q_1–Q_4 and four primary switches Q_5–Q_8). The coupled inductor (T_c) is located between two secondary windings of transformer and connected to the neutral point of the bipolar output. The primary to secondary and tertiary turns ratio of T_r is n:1:1. The self-inductances of the coupled inductor is L_1 and L_2, the turns ratio of which is 1:1. The input voltage is V_{in}, the primary blocking capacitor is C_b, and the voltages across C_{o1} and C_{o2} are V_{o1} and V_{o2}, respectively.

Considering the complexity of the modulation methods, the proposed converter employs a simple single phase-shift (SPS) control strategy as shown in Fig. 4, where the switching frequency is f_s and the switching period is $T_s = 1/f_s$. All switches have the same duty cycle of 0.5, and Q_1 and Q_4 (Q_2 and Q_3) have the same drive signal, as well as Q_5 and Q_8 (Q_6 and Q_7). Q_1 and Q_2 are complementary switched with enough dead time, as well as Q_5 and Q_6.

According to different conditions of load power P_{o1} and P_{o2}, the proposed bipolar converter has three operating modes, namely $P_{o1} < P_{o2}$, $P_{o1} > P_{o2}$, and $P_{o1} = P_{o2}$. Taking $P_{o1} < P_{o2}$ as an example to conduct modal analysis, as shown in Fig. 4(a). Before detailed analyses, the following assumptions are made.

1) T_r is ideal, hence, its leakage inductor can be neglected.
2) The voltage across C_b is much smaller than V_{in}, hence, it can be neglected.
3) C_{o1} and C_{o2} are large enough so that V_{o1} and V_{o2} are constant under steady state.

From Fig. 4(a), one switching period can be divided into eight stages. Due to symmetrical operation, only the four stages within first half switching period from t_0 to t_4 will be analyzed. The corresponding current paths are illustrated in Fig. 5.

Stage 1 [t_0, t_1] [see Fig. 5(a)*]:* At t_0, Q_2 and Q_3 are turned OFF. The primary current i_p charges the junction capacitors of Q_2 and Q_3 and discharges the junction capacitors of Q_1 and Q_4 until the drain–source voltage of Q_1 and Q_4 decays to zero. Then, the body diodes of Q_1 and Q_4 will be conducted to satisfy

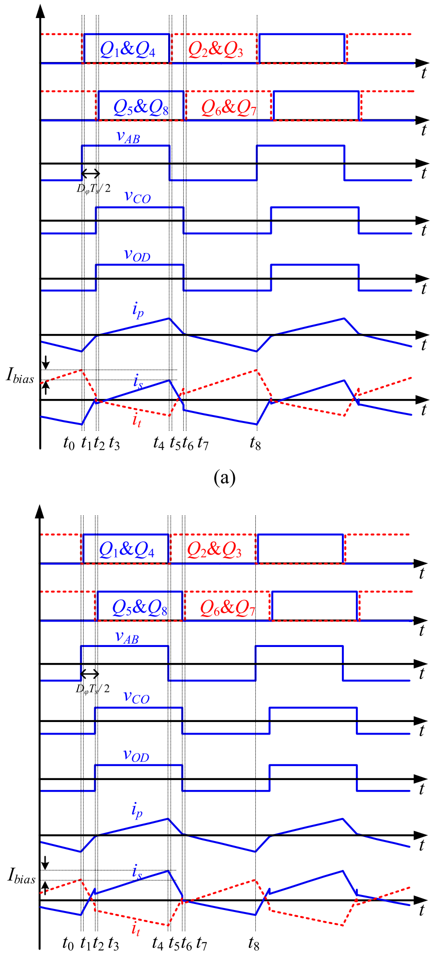

(a)

(b)

Fig. 4. Key waveforms of the proposed converter. (a)$P_{o1} < P_{o2}$. (b) $P_{o1} > P_{o2}$.

the soft-switching condition in the next stage. During this stage, the voltage v_{AB} across nodes A and B increases from–$V_{\rm in}$ to $V_{\rm in}$. For the voltage of C_b is neglected and T_r is ideal, the respective voltages v_s and v_t of secondary and tertiary windings increase from –$V_{\rm in}/n$ to $V_{\rm in}/n$. Since Q_6 and Q_7 are ON, the voltage v_{CO} (v_{OD}) across nodes C (O) and O (D) keeps as –V_{o2} (–V_{o1}).

Stage 2 [t_1, t_2] [see Fig. 5(b)*]:* At t_1, Q_1 and Q_4 are turned ON. Hence, v_{AB} equals to V_{in}, and both v_s and v_t equal to V_{in}/n. Since Q_6 and Q_7 are still ON, v_{CO} and v_{OD} are –V_{o2} and –V_{o1}, respectively. The respective voltages v_{L1} and v_{L2} across L_1 and L_2 can be expressed as follows:

$$\begin{cases} v_{L1} = v_s - v_{CO} = V_{\rm in}/n + V_{o2} \\ v_{L2} = v_t - v_{OD} = V_{\rm in}/n + V_{o1} \end{cases}. \tag{1}$$

Hence, the secondary and tertiary currents i_s and i_t start to increase and decrease linearly, respectively. And i_s and i_t can be expressed as follows:

$$\begin{cases} i_s\left(t\right) = i_s\left(t_1\right) + \frac{V_{\rm in}/n+V_{o2}}{L_1}\left(t - t_1\right) \\ i_t\left(t\right) = i_t\left(t_1\right) - \frac{V_{\rm in}/n+V_{o1}}{L_2}\left(t - t_1\right). \end{cases} \tag{2}$$

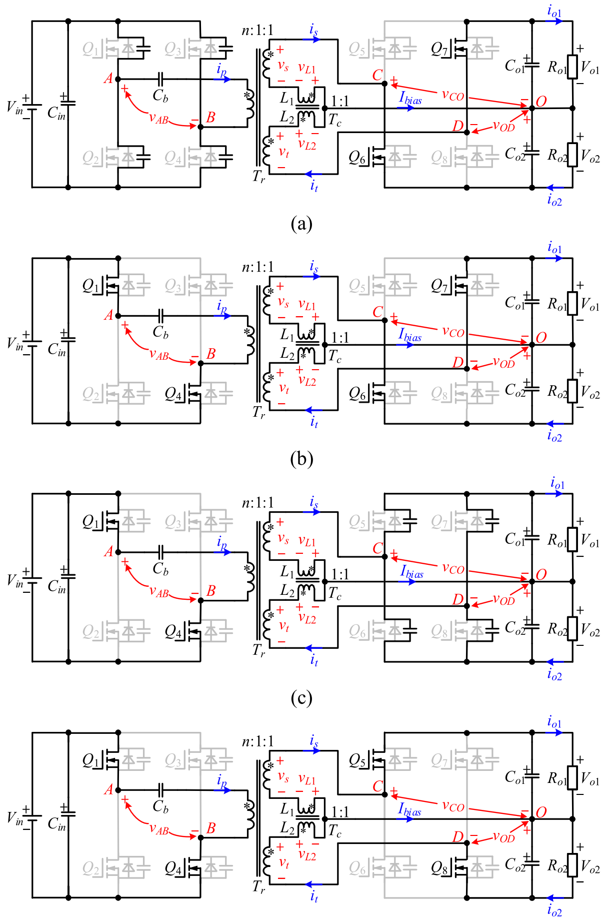

(a)

(b)

(c)

(d)

Fig. 5. Equivalent circuits. (a) [t_0, t_1]. (b) [t_1, t_2]. (c) [t_2, t_3]. (d) [t_3, t_4].

As shown in Fig. 3, when bipolar loads are unbalanced, a dc bias current $I_{\rm bias}$ is generated at the midpoint of the coupled inductor, enabling bipolar voltage balance. Its maximum value is V_{o1}/R_{o1} when the bipolar load with one terminal fully loaded and the other unloaded. When $I_{\rm bias}$>0, it indicates that $P_{\rm o1}$<$P_{\rm o2}$. When $I_{\rm bias}$<0, it indicates that $P_{\rm o1}$>$P_{\rm o2}$. Generally, $I_{\rm bias}$ can flow to the primary side through the transformer T_r. However, due to the effect of blocking capacitor C_b, it turns to flow through the secondary and tertiary windings, which will affect i_s and i_t. Therefore, under different load conditions, the dc component of i_p is always zero, as shown in Fig. 4, which prevents the magnetic saturation of the high-frequency transformer. For the currents on the secondary and tertiary sides, considering the symmetry of the topology, the amplitudes of their dc components are both $I_{\rm bias}$/2. Thereby, when $P_{o1} < P_{o2}$, a positive and a negative dc current are superimposed on i_t and i_s, as shown in Fig. 4(a). Conversely, when $P_{o1} > P_{o2}$, a negative and a positive dc current are superimposed on i_t and i_s, as shown in Fig. 4(b).

Stage 3 [t_2, t_3] [see Fig. 5(c)*]:* At t_2, Q_6 and Q_7 are turned OFF. i_s charges the junction capacitors of Q_6 and discharges the junction capacitors of Q_5 until the drain–source voltage of Q_5 decays to zero. Moreover, i_t charges the junction capacitors of Q_7 and discharges the junction capacitors of Q_8 until the drain–source voltage of Q_8 decays to zero. Then, the body diodes

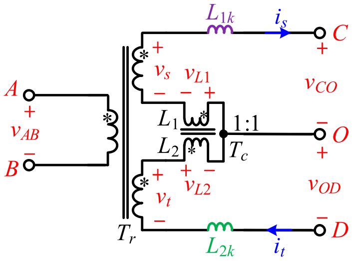

Fig. 6. Equivalent circuit diagram of the converter considering the leakage inductance of the secondary and tertiary sides of the transformer.

of Q_5 and Q_8 will be conducted to satisfy the soft-switching condition in the next stage. During this stage, v_{AB} keeps as V_{in}, v_{CO} (v_{OD}) increases from $-V_{o2}$ ($-V_{o1}$) to V_{o1} (V_{o2}).

Stage 4 [t_3, t_4] [see Fig. 5(b)*]:* At t_3, Q_5 and Q_8 are turned ON. Hence, v_{CO} and v_{OD} are V_{o1} and V_{o2}, respectively. Since Q_1 and Q_4 are still ON, v_{AB} equals to V_{in}, both v_s and v_t equal to V_{in}/n. v_{L1} and v_{L2} can be expressed as follows:

$$\begin{cases} v_{L1} = v_s - v_{CO} = V_{\text{in}}/n - V_{o1} \\ v_{L2} = v_t - v_{OD} = V_{\text{in}}/n - V_{o2}. \end{cases} \tag{3}$$

Hence, i_s and i_t start to increase and decrease linearly, respectively. And i_s and i_t can be expressed as follows:

$$\begin{cases} i_s(t) = i_s(t_3) + \frac{V_{\text{in}}/n - V_{o1}}{L_1}(t - t_3) \\ i_t(t) = i_t(t_3) - \frac{V_{\text{in}}/n - V_{o2}}{L_2}(t - t_3). \end{cases} \tag{4}$$

III. CHARACTERISTICS

A. Automatic Voltage Balancing

According to (1) and (4), it can be concluded that under ideal coupled inductor conditions ($v_{L1} = v_{L2}$), the bipolar voltages are naturally balanced ($V_{o1} = V_{o2}$). However, in practical applications, since coupled inductor are not fully coupled (with the coupling coefficient k less than 1), and transformer windings inherently exhibit leakage inductance, these factors may compromise the voltage balancing capability of the converter. Thus, considering the leakage inductances L_{1k} and L_{2k} of the secondary and tertiary sides of the transformer, the equivalent circuit of the converter is shown in Fig. 6.

Due to the fact that the coupled inductor is adopted, v_{L1} and v_{L2} can be obtained as follows:

$$\begin{cases} v_{L1}(t) = L_1\frac{di_s}{dt} + M\frac{di_t}{dt} \\ v_{L2}(t) = L_2\frac{di_t}{dt} + M\frac{di_s}{dt} \end{cases} \tag{5}$$

where M is the mutual inductance of the proposed coupled inductor.

The coupling coefficient can be obtained from $k = M/\sqrt{L_1 L_2} = M/L_1$ with $L_1 = L_2$. Hence, one can obtain the following:

$$\begin{cases} v_{L1}(t) = L_1\frac{di_s}{dt} + kL_1\frac{di_t}{dt} \\ v_{L2}(t) = L_2\frac{di_t}{dt} + kL_1\frac{di_s}{dt} \end{cases}. \tag{6}$$

As shown in Fig. 6, it can be derived from (1), (6) that

$$V_{\text{in}}/n + V_{o2} = L_1\frac{V_{\text{in}}/n + V_{o2}}{L_1 + L_{1k}} + kL_1\frac{V_{\text{in}}/n + V_{o1}}{L_1 + L_{2k}}. \tag{7}$$

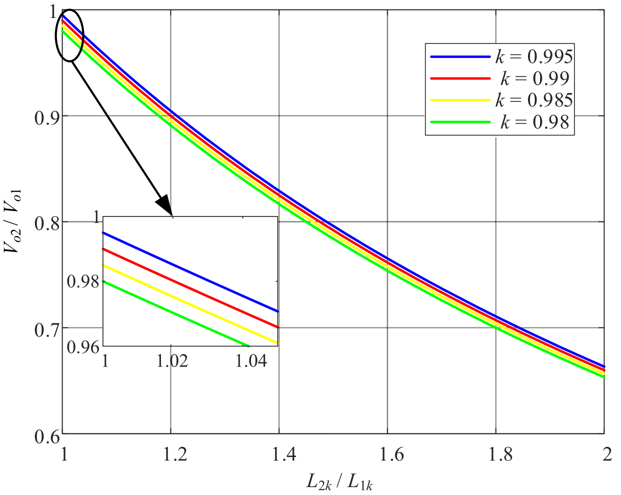

Fig. 7. Voltage balancing capability versus L_{2k}/L_{1k} with different k.

With (7), V_{o2} / V_{o1} can be derived and expressed as follows:

$$\frac{V_{o2}}{V_{o1}} = k\frac{2}{1 + L_{2k}/L_{1k}}. \tag{8}$$

As seen, when the coupled inductors are fully coupled ($k = 1$), and the leakage inductance of the secondary and tertiary sides of the transformer are equal ($L_{1k} = L_{2k}$), the bipolar output voltages are always automatically balanced, regardless of the load conditions at the output ports or the sum of the bipolar dc output voltages. Fig. 7 shows the V_{o2}/ V_{o1} obtained with various k and L_{2k}/ L_{1k}. When the leakage inductance ratio L_{2k}/ L_{1k} is small, a higher coupling coefficient results in better voltage balancing. Generally, the practical k can be higher than 0.985 [18], and L_{2k}/ L_{1k} can be smaller than 1.05, corresponding to V_{o2}/V_{o1} exceeding 96% under operational constraints.

B. Transferred Power Characteristics

When the load is balanced, the secondary current i_s is symmetric about the time axis. Thus, the following expression can be obtained after neglecting the switching dead time:

$$\frac{1}{T_s}\int_{t_0}^{t_8} i_s(t)dt = 0 \tag{9}$$

$$\begin{cases} i_s(t_2) = -i_s(t_6) = i_s(t_0) + \frac{V_{\text{in}}/n + V_{o2}}{L_1} D_\varphi \frac{T_s}{2} \\ i_s(t_4) = -i_s(t_0) = i_s(t_2) + \frac{V_{\text{in}}/n - V_{o1}}{L_1}(1 - D_\varphi)\frac{T_s}{2} \end{cases} \tag{10}$$

where D_φ is the phase-shift duty cycle, and its value is $2\varphi/T_s$.

According to (9) and (10), the following secondary and tertiary current analytical expression can be derived:

$$i_s(t_0) = -i_t(t_0) = \frac{V_{o1} - V_{\text{in}}/n - 2D_\varphi V_{o1}}{4L_1}T_s \tag{11}$$

$$i_s(t_2) = -i_t(t_2) = \frac{V_{o1} - V_{\text{in}}/n + 2D_\varphi V_{\text{in}}/n}{4L_1}T_s. \tag{12}$$

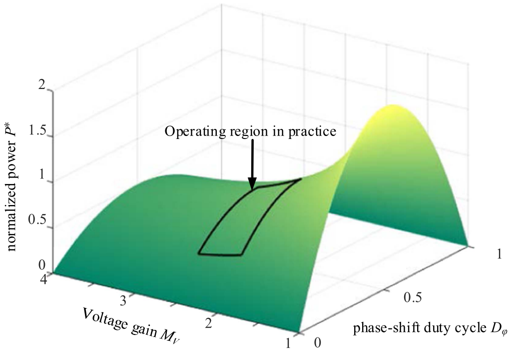

Fig. 8. Transferred power characteristics curve.

Based on the turns ratio relationship, the primary current analytical expression can be derived as follows:

$$i_p(t_0) = \frac{V_{o1} - V_{\text{in}}/n - 2D_\varphi V_{o1}}{4nL_1} T_s \tag{13}$$

$$i_p(t_2) = \frac{V_{o1} - V_{\text{in}}/n + 2D_\varphi V_{\text{in}}/n}{4nL_1} T_s. \tag{14}$$

Based on (13) and (14), the transferred power of the proposed converter can be expressed as follows:

$$P_o = \frac{2}{T_s}\int_{t_0}^{t_4} v_{AB}(t)\, i_p(t)\, dt = \frac{V_{\text{in}} V_{o1}}{2nL_1 f_s} D_\varphi (1 - D_\varphi). \tag{15}$$

P_o is scaled to the normalized power $P^*(P^* = P_o/P_n)$ for better illustration. P_n is shown as follows:

$$P_n = \frac{V_{o1}^2}{8L_1 f_s}. \tag{16}$$

Define the voltage gain M_V as follows:

$$M_V = \frac{2nV_{o1}}{V_{\text{in}}}. \tag{17}$$

According to (15)–(17), P^* is shown as follows:

$$P^* = \frac{8}{M_V} D_\varphi (1 - D_\varphi). \tag{18}$$

Based on (18), the transferred power characteristics curve of the proposed bipolar converter is plotted in Fig. 8. It can be observed that P^* decreases with the increase of M_V. Furthermore, for a fixed M_V, P^* reaches its maximum value. when D_φ equals 0.5. The operating region in practical prototype is designed as the black box in Fig. 8.

C. ZVS Analysis

If the parasitic capacitance of the switch is neglected, whether the switch can achieve ZVS depends only on the polarity of the switch current at the instant of turn-on. Based on the operating stages, the ZVS conditions are summarized in Table I.

TABLE I
ZVS CONDITIONS FOR SWITCHES

Switches	Instant current	Switches	Instant current
Q_1&Q_4	$i_p(t_0) < 0$	Q_6	$i_s(t_6) < 0$
Q_2&Q_3	$i_p(t_4) > 0$	Q_7	$i_t(t_6) > 0$
Q_5	$i_s(t_2) > 0$	Q_8	$i_t(t_2) < 0$

TABLE II
ZVS CONDITIONS FOR SWITCHES

Switches	ZVS condition
Q_1-Q_4	$1 - 2D_\varphi - 2/M_V < 0$
Q_5&Q_7	$2D_\varphi - 1 + M_V/2 - I_{dc} > 0$
Q_6&Q_8	$2D_\varphi - 1 + M_V/2 + I_{dc} > 0$

*$|I_{\text{dc}}| = 2nL_1 I_{\text{bias}}/V_{\text{in}}T_s$.

By substituting (11)–(14) and (18) into Table I, the analytical expression of soft-switching conditions can be obtained. As shown in Table II, I_{dc} represents the degree of load balance, and when $I_{\text{bias}} = V_{o1}/R_{o1}$, its maximum value is $M_V L_1/T_s R_{o1}$. When the bipolar load is balanced (i.e., $I_{\text{dc}} = 0$), substituting (18) into Table II reveals that the ZVS boundaries of the switches under this condition are depicted in Fig. 9(a). Under balanced load operation, the switches on the primary and secondary side exhibit identical ZVS boundaries, respectively. As derived from (18), the operating region in practice of the converter fully resides within the ZVS region.

When the bipolar load is unbalanced, I_{bias} will circulate through the secondary-side switches, leading to a shift in their ZVS regions. As shown in Fig. 9(b), when $P_{o1}<P_{o2}$ (i.e., I_{dc} >0), the ZVS range of Q_6 and Q_8 expands, while that of Q_5 and Q_7 contracts. Conversely, Fig. 9(c) demonstrates that when $P_{o1}>P_{o2}$ (i.e., I_{dc} <0), the ZVS range of Q_5 and Q_7 extends at the expense of the ZVS range of Q_6 and Q_8. For the ZVS range of the primary-side switches, the unbalanced load will not affect the current on the primary side and the ZVS range of the primary-side switches due to C_b. Moreover, even under unbalanced load conditions, the practical operating range is within the ZVS region.

IV. EXPERIMENTAL RESULTS

A. Prototype and Design Consideration

To verify the proposed converter, an experimental prototype with 1-kW rated power is built as shown in Fig. 10, and the parameters of which are listed in Table III. Without loss of generality, V_o is selected as ±190 V for this experiment, and V_o can be adjusted according to (18) based on the requirements.

To achieve ZVS, M_V must be constrained with a defined operational range. With (17), the transformer ratio n should satisfy the following:

$$n = \frac{M_V V_{\text{in}}}{2V_{o1}}. \tag{19}$$

In practical applications, M_V is taken within the range of 2–2.5, the turn ratio n is finally set to be 2.

The coupled inductor is constructed using a double-coil parallel winding to achieve a higher coupling coefficient k and voltage balancing capability. With (15), the self-inductance L_1 can be

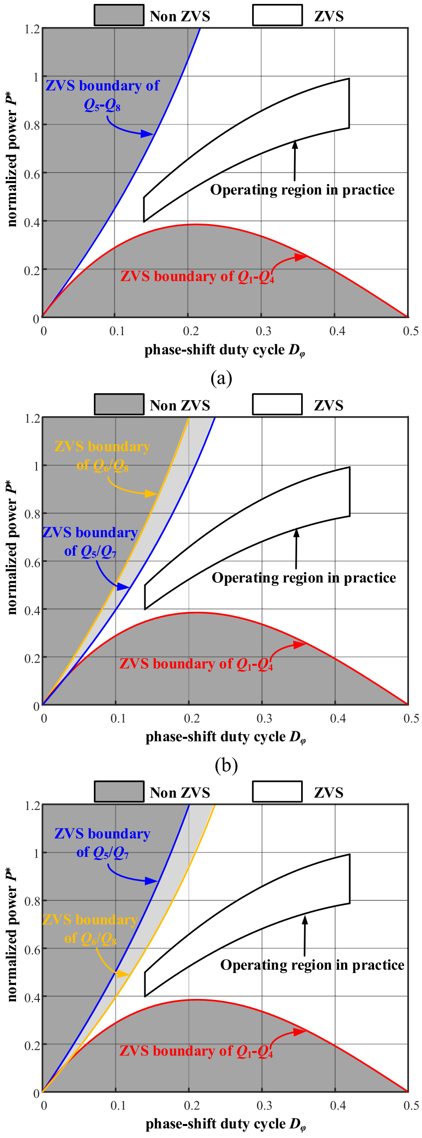

(a)

(b)

(c)

Fig. 9. ZVS region of the switches with different load conditions. (a) $P_{o1} = P_{o2}$. (b) $P_{o1} < P_{o2}$. (c) $P_{o1} > P_{o2}$.

derived

$$L_1 = \frac{V_{\text{in}} V_{o1}}{2n f_s P} D_\varphi \left(1 - D_\varphi\right). \tag{20}$$

A design margin is intentionally reserved by setting $D_\varphi = 0.42$ to ensure the bipolar output operates at full load condition, a self-inductance of 44 μH is chosen.

The presence of the blocking capacitor (C_b) means that no dc component flows through the primary winding of the transformer. To prevent magnetic saturation of the coupled inductor under unbalanced loads, an appropriate air gap must be introduced, the length of which is determined by the following formula:

$$l_g = \frac{\mu_0 N_{L1}^2 A_e}{L_1} \tag{21}$$

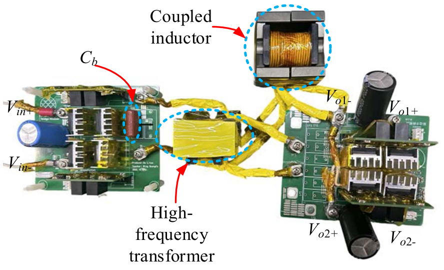

Fig. 10. Experimental prototype.

TABLE III
EXPERIMENTAL PARAMETERS

Parameters	Value
Input voltage (V_{in})	300–380 V
Output voltage (V_{o1}, V_{o2})	190 V
Rated output power (P_o)	1 kW
Turns ratio (n)	2
Blocking capacitor (C_b)	1 μF
Coupled inductors (L_1, L_2)	44 μH
Coupled coefficient (k)	0.99
Secondary/Tertiary leakage inductor (L_{1k}/L_{2k})	1.58 μH/1.52 μH
Switching frequency (f_s)	100 kHz
MOSFETs	IRFPC60PBF

TABLE IV
MAGNETIC COMPONENTS PARAMETERS

Components	Model	l_g(mm)
Transformer (T_r)	PQ5050 N_p: N_s: N_t = 16:8:8	0
Coupled inductor (T_c)	PQ5050 N_{L1}: N_{L2} = 13:13	2.29

where l_g is the length of air gap, N_{L1} is the number of turns on the primary side of the coupled inductor, and A_e is the core cross-sectional area.

The transformer and coupled inductor are designed using the area product method, and the final results are shown in Table IV.

To avoid resonance between C_b and L_1, the resonant frequency of them should be much lower than the switching frequency. The value of C_b is selected to 1 μF based on the following formula:

$$\frac{1}{2n\pi\sqrt{L_1 C_b}} \ll f_s. \tag{22}$$

According to the proposed bipolar converter operation, the voltage stress on the primary-side switches (Q_1-Q_4) and secondary-side switches (Q_5–Q_8) are derived as follows:

$$V_{(Q_1-Q_4)\text{peak}} = V_{\text{in}} \tag{23}$$

$$V_{(Q_5-Q_8)\text{peak}} = V_{o1} + V_{o2}. \tag{24}$$

Based on the steady-state analysis, the peak current and root-mean-square of the primary and secondary-side switches are

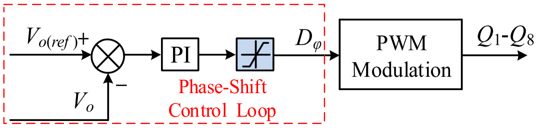

Fig. 11. Control scheme for the proposed bipolar converter.

TABLE V
PARAMETERS OF THREE LOAD CONDITIONS

Conditions	P_{o1}	P_{o2}
A	500 W	0 W
B	0 W	500 W
C	500 W	500 W

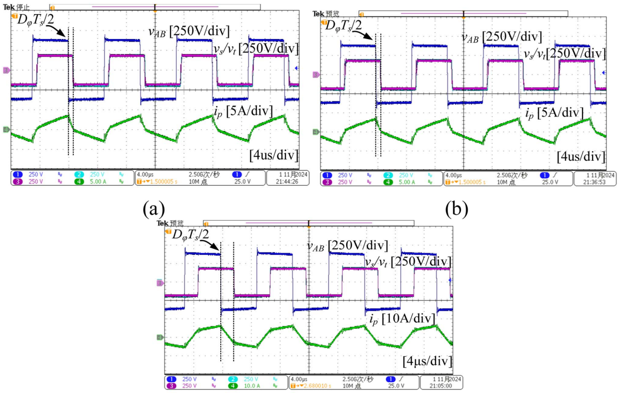

(a) (b) (c)

Fig. 12. Waveforms of v_{AB}, v_s, v_t, and i_p under different bipolar load conditions. (a) Condition A. (b) Condition B. (c) Condition C.

respectively determined as follows:

$$\begin{cases} I_{(Q_1-Q_4)\text{peak}} = \frac{V_{\text{in}}/n+2D_\varphi V_{o1}-V_{o1}}{4nL_1}T_s \\ I_{(Q_5-Q_8)\text{peak}} = \frac{V_{\text{in}}/n+2D_\varphi V_{o1}-V_{o1}}{4L_1}T_s + \frac{V_{o1}}{2R_{o1}} \end{cases} \tag{25}$$

$$\begin{cases} I_{(Q_1-Q_4)\text{RMS}} \approx \frac{I_{(Q_1-Q_4)\text{peak}}}{2\sqrt{3}} \\ I_{(Q_5-Q_8)\text{RMS}} \approx \frac{I_{(Q_5-Q_8)\text{peak}}}{2\sqrt{3}} + \frac{V_{o1}^2}{8R_{o1}^2} \end{cases}. \tag{26}$$

Hence, the MOSFETs IRFPC60PBF with its voltage rating of 600 V and current rating of 16 A are selected.

Fig. 11 illustrates the control strategy diagram of the proposed converter, where a PI controller and SPS modulation is used to regulate the entire output voltage V_o. Finally, the control system is implemented by using the digital signal processor of TMS320F28384.

B. Experimental Evidence

In order to verify the preceding theoretical analysis, where three load conditions are taken for instance, as summarized in Table V: one is that $P_{o1} = 500$ W and $P_{o2} = 0$ W for Condition A, another is that $P_{o1} = 0$ W and $P_{o2} = 500$ W for Condition B, and the other is that $P_{o1} = 500$ W and $P_{o2} = 500$ W for Condition C. Fig. 12 shows the waveforms of v_{AB}, v_s, v_t, and i_p according to different bipolar load conditions. As seen, the phase-shift duty cycle D_φ is adjusted to transfer the total output power, and it can be determined by using (15). Each independent power P_{o1} and P_{o2} does not affect the value of D_φ, because D_φ only determines the entire output power P_o. Therefore, both Condition A and Condition B have the same D_φ. At the same time, the primary-side current i_p has no dc component due to the presence of a blocking capacitor as shown in Fig. 12.

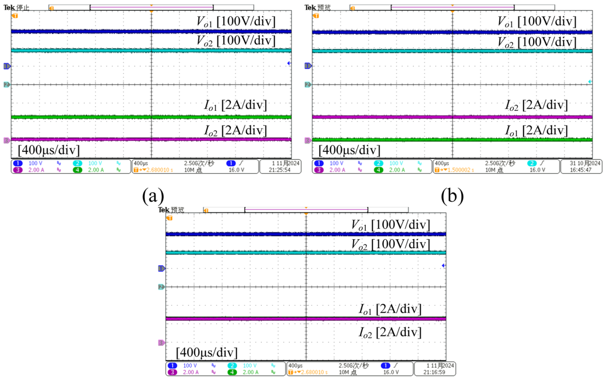

(a) (b) (c)

Fig. 13. Waveforms of V_{o1}, V_{o2}, I_{o1}, and I_{o2} under different bipolar load conditions. (a) Condition A. (b) Condition B. (c) Condition C.

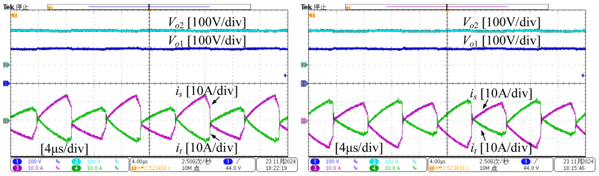

(a) (b)

Fig. 14. Waveforms of i_s and i_t under unbalanced load conditions. (a) Condition A. (b) Condition B.

The key waveforms of V_{o1}, V_{o2}, I_{o1}, and I_{o2} under different bipolar load conditions are shown in Fig. 13. As can be seen, under different load conditions, the experimental prototype keeps $V_{o1} = V_{o2}$ at a constant value of 190 V. Therefore, the proposed converter has a good voltage balancing performance. Fig. 14 shows the waveforms of secondary current of the transformer under different bipolar load conditions. In Fig. 14(a), the conditions A is presented, where 250 W is unbalanced between two output ports. To balance bipolar voltage, i_s and i_t have a dc component with positive and negative polarity, respectively, which ensure that the I_{bias} is negative polarity and provides an additional 250 W of power to the V_{o1} side, thereby, finally having 500 W at the V_{o1} side and 0 W at the V_{o2} side. In Fig. 14(b), the bipolar load condition is opposite to the case of Fig. 14(a). Therefore, the dc components of i_s and i_t are negative and positive polarity, respectively, which can distribute 500 W to the V_{o2} side.

In order to verify the dynamic performance, Fig. 15(a) and (c) shows the waveforms varies from 380 to 300 V and back to 380 V under $P_{o1} = 500$ W, $P_{o1} = 0$ W, and $P_{o1} = 500$ W, P_{o1} = 250 W, respectively. Fig. 15(b) shows the waveforms under $V_{\text{in}} = 380$ V, where the V_{o2} port operates under full load, while

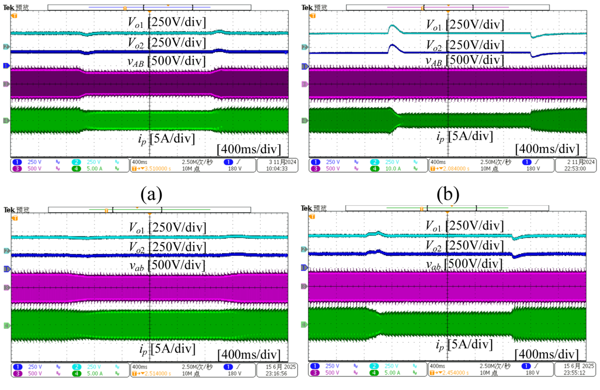

(a) (b) (c) (d)

Fig. 15. Dynamic waveforms. (a) V_{in} varies from 380 to 300 V and back to 380 V under $P_{o1} = 500$ W, $P_{o2} = 0$ W. (b) $P_{o1} = 500$ W, P_{o2} varies from 500 to 0 W and back to 500 W under $V_{\text{in}} = 380$ V. (c) V_{in} varies from 380 to 300 V and back to 380 V under $P_{o1} = 500$ W, $P_{o2} = 250$ W. (d) $P_{o1} = 500$ W, P_{o2} varies from 250 to 0 W and back to 250 W under $V_{\text{in}} = 380$ V.

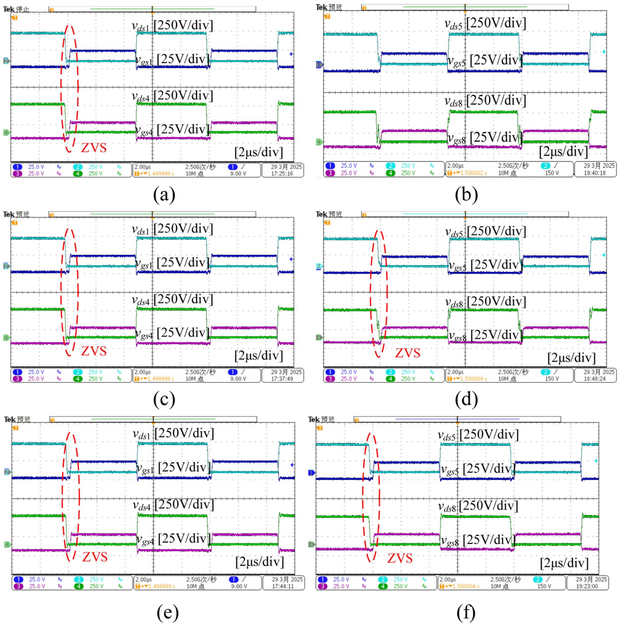

(a) (b) (c) (d) (e) (f)

Fig. 16. Experimental waveforms of ZVS results under different load conditions. (a) Q_1 and Q_4 under Condition A. (b) Q_5 and Q_8 under Condition A. (c) Q_1 and Q_4 under Condition B. (d) Q_5 and Q_8 under Condition B. (e) Q_1 and Q_4 under Condition C. (f) Q_5 and Q_8 under Condition C.

the V_{o1} port is from full load to no load and back to full load. Fig. 15(d) shows the waveforms under $V_{\text{in}} = 380$ V, where the V_{o2} port operates under full load, while the V_{o1} port is from full load to half load and back to half load. As can be seen, the bipolar voltages are balanced all the time, and have a good dynamic performance as well. In summary, the experimental results verify that the bipolar voltages remain balanced with a good dynamic performance even when an input voltage or load sudden change occurs.

To verify the effects of varying load conditions on ZVS performance, Fig. 16 shows the ZVS waveforms of Q_1, Q_4, Q_5, and Q_8 under different load conditions, it can be clearly seen that all switches can achieve ZVS-on. As shown in Fig. 16(a), (c) and (e), Q_1 and Q_4 exhibit identical ZVS ranges across varying load conditions owing to the blocking capacitor's presence. Combined with Fig. 16(b), (d) and (f), it can be observed that the ZVS range of the secondary-side switches exhibits slight differences under different load conditions. Under Condition A (with negative I_{dc}), the ZVS range of Q_5 diminishes while that of Q_8 expands. The converse situation is observed under Condition B. In contrast, under condition C, Q_5 and Q_8 achieve identical ZVS conditions. For the symmetry of the proposed converter, the remaining switches Q_2, Q_3, Q_6, and Q_7 can also obtain the ZVS-on.

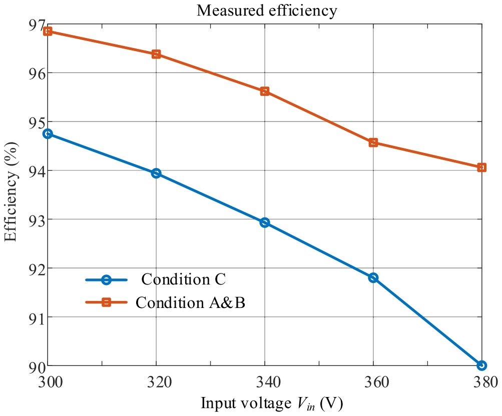

Fig. 17. Measured efficiency curves of full load and half load under different input voltage V_{in}.

Fig. 17 shows the measured experimental efficiencies under various load conditions and input voltages, while the entire output voltage V_o maintains 380 V. The orange curve depicts the converter efficiency with varying V_{in} under Condition C. It can be seen the conversion efficiency drops from 96.75% to 94.06% when V_{in} increases from 300 to 380 V. The results show the efficiency of proposed converter decreases with the increase of V_{in} under the same load condition. Also, experimental efficiency under Conditions A and B indicated by the blue curve changes from 94.75% (at $V_{\text{in}} = 300$ V) to 90% (at $V_{\text{in}} = 380$ V). Noted that the all the two curves show similar curvilinear trend. In addition, by comparing the two curves, it can be seen under the same input voltage V_{in}, the efficiency at full load is higher than at half load.

The histogram of theoretical losses under different load conditions is shown in Fig. 18. As can be seen, the turn OFF losses and the conduction losses decrease with the increase of V_{in}. However, due to there are two magnetic components (including transformer and coupled inductor), the proportion of magnetic losses is relatively large, as shown in Fig. 18. When the input voltage increases, the rate of change of magnetic flux (ΔB) increases, leading to losses increase in the magnetic components. As a result, as the power level increases, the efficiency of the converter decreases.

C. Comparison

The proposed converter is compared with various bipolar dc–dc converters, and the results are summarized in Table VI. Compared to the topology in papers [16] and [22], the key advantage of the proposed converter is that it achieves bipolar

TABLE VI
COMPARISON OF THE PROPOSED CONVERTER WITH OTHER SIMILAR SOLUTIONS

Topologies		[16]	[18]	[22]	[23]	[24]	[25]	Proposed converter
Number of devices	S	2	4	16	6	12	12	8
	D	4	8	0	0	0	0	0
	C	4	2	4	5	3	3	4
	L	1 + 1(CI)	1(CI)	0	2	0	1(CI)	1(CI)
	T	0	1	3	1	1	1	1
Voltage conversion ratio		$D/(1-D)^2$& $(n+D-1)/(1-D)^2$	nD	G_{DAB}	$2n/(1-D)$	G_{TAB}	G_{TAB}	G_{DAB}
Soft switching		/	ZVS	ZVS	Full-range ZVS	/	ZVS	ZVS
Rating power		210 W	1 kW	144 W	5 kW	4 kW	5 kW	1 kW
Frequency		50 kHz	100 kHz	20 kHz	20 kHz	25 kHz	20 kHz	100 kHz
Efficiency		93.3%	/	92.4%	96.2%	/	/	96.8%
Electrical isolation		No	Yes	Yes	Yes	Yes	Yes	Yes
Voltage self-balancing		No	Yes	No	Yes	Yes	Yes	Yes

Note: S, switch; D, diode; C, capacitor; L, inductor; T, transformer; CI, coupled inductor; $G_{\mathrm{DAB}}/G_{\mathrm{TAB}}$, voltage conversion ratio of dual active bridge converter/triple active bridge converter.

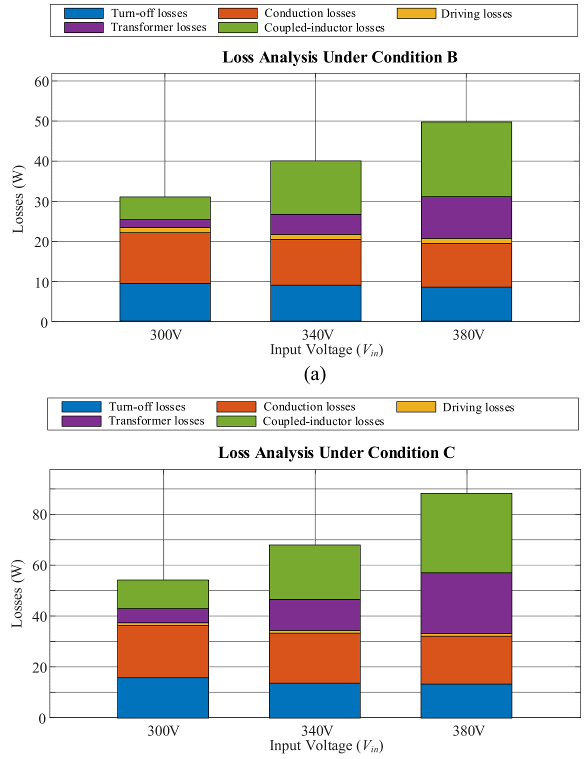

(a)

(b)

Fig. 18. Theoretical loss calculation results of different load balancing condition. (a) Condition B. (b) Condition C.

voltage self-balancing, which can automatically balance two output voltages under unbalanced load conditions without requiring additional voltage balancing control. In comparison to the voltage self-balancing topology proposed [22] and [23], the proposed converter has fewer magnetic devices, which can reduce magnetic core loss. Additionally, compared with the converters in papers [22], [24], and [25], the proposed converter reduces the number of switches, thereby lowering the complexity of the driving and control circuits. Furthermore, in comparison with the topology in [18], the proposed converter improves the efficiency by achieving ZVS for all switches, while paper [18] suffers from hard-switching losses in its diodes. As a result, the proposed bipolar converter has advantages over the existing bipolar methods.

V. CONCLUSION

This article proposed the DAB based self-balancing converter with coupled inductor, which can balance bipolar voltages under any load conditions. At the same time, the coupled inductor provides the required inductance for power transfer. It enables ZVS for all switches under different load conditions, which helps in reducing switching losses. Additionally, the simple single phase-shift modulation can be used, which is simple and familiar to engineers. Compared to other bipolar solutions, the proposed converter has fewer semiconductors and magnetic components, which can increase the efficiency of the converter. The theoretical analysis and characteristics are well verified by the experimental results.

REFERENCES

[1] W. Sun and G. P. Harrison, “Wind-solar complementarity and effective use of distribution network capacity,” *Appl. Energy*, vol. 247, pp. 89–101, Aug. 2019.

[2] J. Lago, J. Moia, and M. L. Heldwein, “Evaluation of power converters to implement bipolar DC active distribution networks — DC-DC converters,” in *Proc. IEEE Energy Convers. Congr. Expo.*, 2011, pp. 985–990.

[3] Y. Chen, J. Ma, M. Zhu, and Y. Li, “Bipolar semiactive bridge converter with cross-cycle modulation for resilience enhancement in bipolar DC distribution systems,” *IEEE J. Emerg. Sel. Topics Power Electron.*, vol. 12, no. 3, pp. 2406–2418, Jun. 2024.

[4] Y. Gu, W. Li, and X. He, “Analysis and control of bipolar LVDC grid with DC symmetrical component method,” *IEEE Trans. Power Syst.*, vol. 31, no. 1, pp. 685–694, Jan. 2016.

[5] G. V. den Broeck, W. Martinez, M. Dalla Vecchia, S. Ravyts, and J. Driesen, “Conversion efficiency of the buck three-level DC–DC converter in unbalanced bipolar DC microgrids,” *IEEE Trans. Power Electron.*, vol. 35, no. 9, pp. 9306–9319, Sep. 2020.

[6] H. Kakigano, Y. Miura, T. Ise, and R. Uchida, “DC voltage control of the DC micro-grid for super high quality distribution,” in *Proc. Power Convers. Conf.*, 2007, pp. 518–525.

[7] X. Zhang and C. Gong, “Dual-buck half-bridge voltage balancer,” *IEEE Trans. Ind. Electron.*, vol. 60, no. 8, pp. 3157–3164, Aug. 2013.

[8] X. Zhang, C. Gong, and Z. Yao, “Three-level DC converter for balancing DC 800-V voltage,” *IEEE Trans. Power Electron.*, vol. 30, no. 7, pp. 3499–3507, Jul. 2015.

[9] S. D. Tavakoli, M. Mahdavyfakhr, M. Hamzeh, K. Sheshyekani, and E. Afjei, "A unified control strategy for power sharing and voltage balancing in bipolar DC microgrids," *Sustain. Energy, Grids Netw.*, vol. 11, pp. 58–68, Sep. 2017.

[10] H. Kang and H. Cha, "A new nonisolated high-voltage-gain boost converter with inherent output voltage balancing," *IEEE Trans. Ind. Electron.*, vol. 65, no. 3, pp. 2189–2198, Mar. 2018.

[11] P. Prabhakaran and V. Agarwal, "Novel boost-sepic type interleaved DC–DC converter for mitigation of voltage imbalance in a low-voltage bipolar DC microgrid," *IEEE Trans. Ind. Electron.*, vol. 67, no. 8, pp. 6494–6504, Aug. 2020.

[12] B. Rooholahi, Y. P. Siwakoti, H.-G. Eckel, F. Blaabjerg, and A. S. Bahman, "Enhanced single-inductor single-input dual-output DC–DC converter with voltage balancing capability," *IEEE Trans. Ind. Electron.*, vol. 71, no. 7, pp. 7241–7251, Jul. 2024.

[13] X. Zhou, Y. Wang, L. Wang, Y.-F. Liu, and P. C. Sen, "A soft-switching transformerless DC−DC converter with single-input bipolar symmetric outputs," *IEEE Trans. Power Electron.*, vol. 36, no. 8, pp. 8640–8646, Aug. 2021.

[14] J.-Y. Lee, H.-S. Kim, and J.-H. Jung, "Enhanced dual-active-bridge DC–DC converter for balancing bipolar voltage level of DC distribution system," *IEEE Trans. Ind. Electron.*, vol. 67, no. 12, pp. 10399–10409, Dec. 2020.

[15] V. F. Pires, A. Cordeiro, D. Foito, and J. F. A. Silva, "Dual output and high voltage gain DC-DC converter for PV and fuel cell generators connected to DC bipolar microgrids," *IEEE Access*, vol. 9, pp. 157124–157133, 2021.

[16] S. Hasanpour and T. Nouri, "New coupled-inductor high-gain DC/DC converter with bipolar outputs," *IEEE Trans. Ind. Electron.*, vol. 71, no. 3, pp. 2601–2613, Mar. 2024.

[17] B. Li et al., "DC/DC converter for bipolar LVdc system with integrated voltage balance capability," *IEEE Trans. Power Electron.*, vol. 36, no. 5, pp. 5415–5424, May 2021.

[18] G. Ning, J. Chen, Y. Liu, G. Xu, W. Xiong, and M. Su, "Coupled-inductor-based buck-type converter with autonomous voltage balancing for bipolar DC microgrid," *IEEE Trans. Power Electron.*, vol. 39, no. 10, pp. 11937–11942, Oct. 2024.

[19] Y. Lin, F. Zhou, G. Xu, W. Xiong, and G. Ning, "Bipolar current-fed DC–DC converter with automatic voltage balance and full range ZVS for bipolar DC system," *IEEE Trans. Power Electron.*, vol. 39, no. 4, pp. 4248–4259, Apr. 2024.

[20] Q. Ren, Y. Han, M. Zhou, C. Yan, P. Yang, and C. Wang, "Overview of voltage balancing schemes in bipolar DC microgrids," *IEEE Trans. Power Electron.*, vol. 40, no. 2, pp. 3469–3489, Feb. 2025.

[21] J.-S. Hong, J.-I. Ha, S. Cui, and J. Hu, "Topology and control of an enhanced dual-active bridge converter with inherent bipolar operation capability for LVDC distribution systems," *IEEE Trans. Power Electron.*, vol. 38, no. 10, pp. 12774–12789, Oct. 2023.

[22] X. Fang, F. Liu, X. Diao, Y. Huang, H. Zhu, and X. Zha, "An isolated four-port voltage self-balancing converter for bipolar DC microgrids," *IEEE Trans. Ind. Electron.*, in early access, doi: 10.1109/TIE.2025.3569969.

[23] G. Ning, H. Pi, H. Han, Y. Liu, Y. Sun, and M. Su, "Automatic voltage-balancing DC–DC converter with wide voltage gain and full range ZVS for bipolar DC microgrids," *IEEE Trans. Power Electron.*, vol. 40, no. 8, pp. 10469–10480, Aug. 2025.

[24] S. Lee, H. Cha, and D.-C. Lee, "Voltage balancing for triple-active-bridge converter using integrated transformer," *IEEE J. Emerg. Sel. Topics Power Electron.*, vol. 13, no. 2, pp. 2027–2035, Apr. 2025.

[25] N. Naseem and H. Cha, "Triple-active-bridge converter with automatic voltage balancing for bipolar dc distribution," *IEEE Trans. Power Electron.*, vol. 37, no. 7, pp. 8640–8648, Jul. 2022.

Guangfu Ning (Member, IEEE) was born in Jiangxi, China, in 1992. He received the B.S. degree from the University of Shanghai for Science and Technology, Shanghai, China, in 2014, and the Ph.D. degree from Southeast University, Nanjing, China, in 2020, both in electrical engineering.

He is currently an Associate Professor with the School of Automation, Central South University, Changsha, China. His research interests include the full-bridge converters, soft-switching technique, and high-power high-voltage dc–dc converters in MVDC collection systems.

Ribo Zhang (Graduate Student Member, IEEE) was born in Jilin, China, in 2002. He received the B.S. degree in electrical engineering and automation from Yanshan University, Qinhuangdao, China, in 2024. He is currently working toward the M.S. degree in the School of Automation, Central South University, Changsha, China.

His research interests include dc–dc converters, and soft-switching technique.

Li Jiang (Member, IEEE) was born in Hunan, China, in 1991. He received the B.S. degree in control science and engineering from the Hunan University of Technology, Zhuzhou, China, in 2015, the M.S. degree in control science and engineering from Central South University, Changsha, China, in 2018, and the Ph.D. degree in electrical engineering from Hunan University, Changsha, in 2022.

His research interests include bidirectional dc/dc converters solid-state transformers, and modeling, and charging strategy for Li-ion battery.

Yonglu Liu (Member, IEEE) was born in Chongqing, China, in 1989. He received the B.S., M.S., and Ph.D. degrees from Central South University, Changsha, China, in 2012, 2015, and 2017, respectively, all in electrical engineering.

He is currently a Professor with the School of Automation, Central South University. His research interests include power electronics and renewable energy power conversion systems.

Yao Sun (Member, IEEE) was born in Hunan, China, in 1981. He received the B.S. and M.S. degrees in electrical engineering and the Ph.D. degree in control theory and control engineering from Central South University, Changsha, China, in 2004, 2007, and 2010, respectively.

He has been a Professor with the School of Automation, Central South University. His research interests include matrix converter, microgrid, and wind energy conversion system.

Mei Su (Member, IEEE) was born in Hunan, China, in 1967. She received the B.S. degree in automation, the M.S. degree in control science and engineering, and the Ph.D. degree in control science and engineering from the School of Information Science and Engineering, Central South University, Changsha, China, in 1989, 1992 and 2005, respectively.

She has been a Full Professor with the School of Automation, Central South University. She is currently an Associate Editor for IEEE TRANSACTIONS ON POWER ELECTRONICS. Her research interests include matrix converter, adjustable speed drives, and wind energy conversion system